Use of combined polarization-sensitive optical coherence tomography and Mueller matrix imaging for the polarimetric characterization of excised biological tissue

Joseph Chue-Sang
Yuqiang Bai
Susan Stoff
David Straton
Sharan Ramaswamy
Jessica C. Ramella-Roman

SPIE.

Use of combined polarization-sensitive optical coherence tomography and Mueller matrix imaging for the polarimetric characterization of excised biological tissue

Joseph Chue-Sang,[a] Yuqiang Bai,[a] Susan Stoff,[a] David Straton,[a] Sharan Ramaswamy,[a] and Jessica C. Ramella-Roman[a,b,*]
[a]Florida International University, Department of Biomedical Engineering, 10555 West Flagler Street, EC 2600, Miami, Florida 33174, United States
[b]Florida International University, Herbert Wertheim College of Medicine, 11200 SW 8th Street, AHC2, Miami, Florida 33199, United States

Abstract. Mueller matrix polarimetry and polarization-sensitive optical coherence tomography (PS-OCT) are two emerging techniques utilized in the assessment of tissue anisotropy. While PS-OCT can provide cross-sectional images of local tissue birefringence through its polarimetric sensitivity, Mueller matrix polarimetry can be used to measure bulk polarimetric properties such as depolarization, diattenuation, and retardance. To this day true quantification of PS-OCT data can be elusive, partly due to the reliance on inverse models for the characterization of tissue birefringence and the influence of instrumentation noise. Similarly for Mueller matrix polarimetry, calculation of retardance or depolarization may be influenced by tissue heterogeneities that could be monitored with PS-OCT. Here, we propose an instrument that combines Mueller matrix polarimetry and PS-OCT. Through the co-registration of the two systems, we aim at achieving a better understanding of both modalities. © 2016 Society of Photo-Optical Instrumentation Engineers (SPIE) [DOI: 10.1117/1.JBO.21.7.071109]

1 Introduction

Polarized light imaging has been used in the biomedical field for many years.[1] It has been applied to reveal the border of skin cancer and improve image resolution via removal of multiply scattered light through a degree of polarization (DOP) imaging scheme[2–4] as well as removing multiply scattered light and surface reflection by combining co- and cross-polarized images.[5] Polarization imaging has been combined with spectroscopy in order to image tissue below the surface by discriminating the difference in penetration depth associated with different wavelengths of light. Similar principles have been used to enhance surface capillary contrast.[6,7] Circularly polarized light has been used to investigate the concentration and size of scattering particles in a medium based off of the backscattered light that is retrieved and modeled in a Poincaré sphere using Stokes vectors.[8] Polarization-sensitive Monte Carlo simulations have been developed to model polarized light travel through scattering and birefringent media.[8–10]

Birefringent proteins such as collagen fibrils and muscle fibers are often found preferentially aligned in bundles when serving as load-bearing structures.[11,12] In contrast, in the case of healthy epidermis, collagen is randomly aligned.[13–15] Significant changes in optical anisotropy and thus birefringence can point to damage or disorder of the normal structure of these tissues.[16,17] We have shown that the degree of circular polarization is particularly sensitive to the dominant orientation of birefringent

bundles such as collagen.[18] In-depth information on a material's effects on polarized light can also be inferred from the calculation of its Mueller matrix.[19] Mueller matrix imaging is possibly the most useful of all polarimetry techniques as the 4×4 Mueller matrix completely characterizes the polarimetric properties of a sample[17] including its cellular size distribution and refractive index.[20] MM decomposition is used to extract constituent polarization properties of an unknown complex system. The decomposition of the Mueller matrix M, whose terms are shown in Eq. (1) (as proposed by Lu and Chipman[21]) yields three canonical matrices of Eq. (2), a diattenuator matrix MD includes the effects of linear and circular diattenuation, M_Δ accounting for the depolarizing effects of the material, and a retarder matrix MR for the effects of the material linear birefringence and optical activity. By decomposing M we are able to isolate different light/tissue interaction mechanism, such as scattering, absorption, chirality, and cumulative retardance. Furthermore, the resulting matrices can be analyzed to yield quantitative medium properties that have a demonstrated[6,22,23] useful diagnostic power and will be used in this study. These parameters are depolarization, linear retardance (birefringence), optical rotation, slow axis orientation θ (the direction of polarization with the larger optical index), and diattenuation D. Depolarization is caused by multiple scattering events and is prominent in biological tissue.[24] It results in the randomization of the polarization of light that travels through scattering media.

*Address all correspondence to: Jessica C. Ramella-Roman, E-mail: jramella@fiu.edu

$$M = \begin{bmatrix} m_{00} & m_{01} & m_{02} & m_{03} \\ m_{10} & m_{11} & m_{12} & m_{13} \\ m_{20} & m_{21} & m_{22} & m_{23} \\ m_{30} & m_{31} & m_{32} & m_{33} \end{bmatrix}, \tag{1}$$

$$M = M_{\Delta} M_{\mathrm{R}} M_{\mathrm{D}}. \tag{2}$$

These parameters can be used to identify tissue changes due to injury or disease.[25] Equation (2) is one of six possible decompositions and the most commonly used in biomedical application. Despite these many applications and some interesting computational work polarized light imaging has had limited commercial success in the biomedical field due to a number of factors: light polarization is quickly lost in heavy-scattering media such as biological tissue, analyzing and extracting meaning from heterogeneous tissue is complicated, and there are still limited amounts of data describing polarization properties of tissues.[1,19,26,27]

Optical coherence tomography (OCT) is a noncontact, non-invasive interferometric technique allowing cross-sectional imaging of tissues at the micron level. OCT has been explored in many applications over the past decade, including ophthalmology, cardiovascular, oncology, and dermatology[28–31] as well as embryogenesis, angiogenesis, and tissue engineering.[32–36] Polarization-sensitive OCT (PS-OCT),[37,38–40] as a functional extension of OCT, uses the information encoded in the polarization state of the recorded interference fringe intensity to provide additional contrast. In birefringent materials, a phase delay between the two orthogonally polarized wave components is caused by the difference of the refractive indices n_o and n_e of the ordinary and extraordinary wave $\Delta n = n_o - n_e$, resulting in different phase velocities of both wave components.[41–43] In general, the delay causes an elliptical polarization state, a measure of the internal birefringence. The ellipticity of the signal is recorded by the two detectors measuring the horizontally and vertically polarized interference signal. The double-pass phase retardance between the two components can be calculated through the amplitude ratio of both detected signals

$$\varphi(x, z) = \arctan \frac{|a_2(x, z)|}{|a_1(x, z)|}, \tag{3}$$

where a_1 and a_2 denote the intensity of the horizontal and vertical components of the interference signal, respectively. ϕ denotes the wrapped phase retardance and could be exploited to generate a retardance image. PS-OCT provides high resolution of spatial information pertaining to imaged tissues otherwise not discernible using existing diagnostic optical methods. Nevertheless, PS-OCT results are highly susceptible to low signal-to-noise ratio (SNR),[44,45–47] and values of birefringence obtained with these systems still rely on ad-hoc models.[41,48]

To study the effect of polarized light transfer in heterogeneous biological media, we have developed a system integrating Mueller matrix polarimetry (MMP) and PS-OCT. The multimodal combination of MMP with PS-OCT will provide comprehensive information about optical properties of tissue. Correlation of bulk properties obtained from MMP and detailed structure information from PS-OCT will enhance our interpretation and analysis of imaging data from the targeted tissues, and will refine our understanding of polarized light propagation through turbid media.

2 Materials and Methods

A schematic of the combined PS-OCT and MMP system is shown in Fig. 1. The experimental setup of the high-resolution PS-OCT system is based on a free-space Michelson interferometer and is detailed with the red light path. The system has a resolution of 3.3 μm in air and 2.5 μm in tissue. The laser light source is a broadband superluminescent diode (Bayspec, San Jose, California) with 840 nm central wavelength and 50 nm full width half maximum. Light from the source is split into the sample arm and the reference arm by an 50/50 cube beam splitter. Along the sample path, the light then passes through a quarter-wavelength plate (QWP) at 45 deg and a telecentric scan lens (LSM03-BB, Thorlabs, Newton, New Jersey) focuses signal light onto the sample and collects the backscattered light. A galvanometer-mounted mirror on the sample arm enables transverse beam scanning on the sample. After the beam splitter,
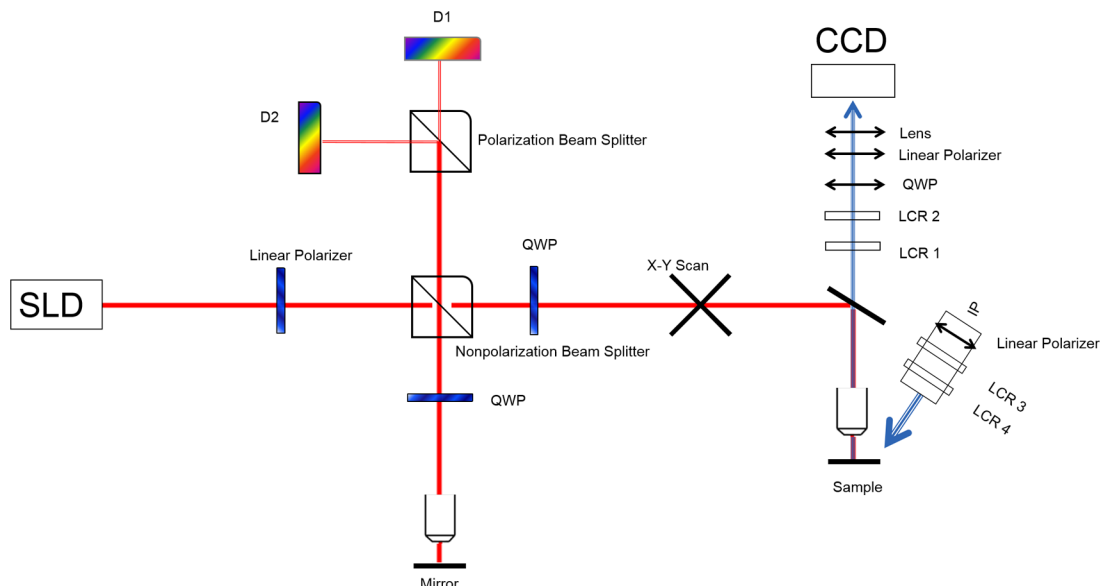

Fig. 1 Combined PS-OCT and Mueller matrix polarimeter schematic.

the beam passes through a QWP @ 22.5 and a scan lens and is then reflected by a reference mirror. A variable attenuator is placed in front of the reference mirror to attenuate light returning from the reference arm. The attenuator is adjusted to optimize the modulation depth of the raw OCT interference term.

Subsequently, both the probe and the reference beams enter a polarization beam splitter, which spatially separates the horizontal and vertical polarization components of these two beams. The spectrum of these two components is simultaneously detected by two custom-made spectrometers consisting of a collimating lens with a focal length of 75 mm (Edmund Optics, Barrington, New Jersey), a 1800 lines/mm volume holography transmission grating (Wasatch Photonics, Logan, Utah), an assembly of triple lenses with an effective focal length of 150 mm, and a line array CCD camera (spL4096-140k, Basler, Highland, Illinois). The acquired interference spectrum data are transferred to a computer system using a National Instrument image acquisition card (PCI 1433). Data processing algorithm, control, and display software are developed using LabView (National Instruments, Austin, Texas). During lateral scanning of the illumination beam on the sample, multiple A-scans are acquired and processed. At the end of the scanning cycle, an intensity-based cross-sectional image (B-scan) of the sample is reconstructed and displayed on the computer screen.

In Fig. 1, the Mueller matrix system is detailed with the blue light path. A CCD camera (Evolve Delta, Photometrics, Tucson, Arizona) with a 0.60× microscope lens (HRD060-NIK, Diagnostic Instruments) attached was secured above the sample objective to allow focusing on the height adjustable stage. A linear polarizer (Prinz, Northbrook, Illinois) and two liquid crystal retarders (LCRs; Meadowlark Optics, Frederick, Colorado) between the lens and sample objective form the PSA of the polarimeter. Employing the same sample objective for the two imaging systems ensures they are imaging the same region of interest. IP in Fig. 1 indicates the light source arm for the MMP. An 530 nm LED (M530L, Thorlabs, Newton, New Jersey) was oriented to illuminate the sample at an incident angle of 45 deg and collimated with a 30 mm diameter tube and a 25 mm diameter plano-convex lens (Newport, Irvine, California). The incident light was linearly polarized (LPVIS100, Thorlabs, Newton, New Jersey) and then retarded using two LCRs before reaching the sample to create four different polarization states. These four different states were then used to calculate the Mueller matrix of the sample. MATLAB (Mathworks, Natick, Massachusetts) was used to control the devices and analyze the data acquired by the MMP which had a field of view of 3 mm and a resolution of 5.8 μm using the shared sample objective.

2.1 Calibration of PS-OCT-Mueller Matrix and Co-Registration of Images

The calibration of the MMP system follows a standard methodology utilized by our group in several applications.[49,50] An Ag-coated mirror was tilted beneath the sample objective on the stage and adjusted so that the maximum intensity of light was reflected from the source into the analyzer above the objective. For calibration, the IP was adjusted to contain a motor-controlled linear polarizer and a QWP in series after the LED light source. Six images were taken with the polarimeter using six different retardances programmed into the LCRs as the linear polarizer's optic axis was rotated between 0 deg and 180 deg with a step size of 10 deg. Four images with different retardances are the minimum required to generate a four-element Stokes vector; however, six images were used in order to increase the accuracy of the calibration matrix generated after the imaging process. The order of the linear polarizer and the QWP was then reversed before repeating the same imaging process. The imaging process and the algorithm for calibrating the MMP using the images taken are discussed in detail in a previous publication.[51]

In order to validate the Mueller matrix function of the MMP, air was used as the standard. The same imaging process used previously for the MMP calibration was again used before constructing a Mueller matrix. Similar to constructing Stokes vectors, four Stokes vectors are the minimum amount of data required to construct a 16-element Mueller matrix. Having more information as the imaging process used did allow for more accurate results. The Mueller matrix of air calculated from images taken from the MMP system are shown below. The error is 0.40% from the ideal Mueller matrix of air.

$$\begin{bmatrix} 0.997 & -0.000 & 0.001 & -0.005 \\ 0.004 & 0.100 & 0.010 & -0.001 \\ -0.001 & 0.004 & 0.991 & 0.002 \\ 0.001 & -0.002 & 0.009 & 0.999 \end{bmatrix}$$

To evaluate our PS-OCT system and to test its effect on the polarization of light returning to the spectrometers, we placed a QWP in front of a mirror onto a rotational stage. The optic axis of the QWP was varied from 0 deg to 180 deg in steps of 10 deg. Its phase retardance was calculated at each position. Figure 2 shows the plot of phase retardance as the optic axis of the QWP was rotated. The standard deviation of the measured phase retardances was 0.89 deg which demonstrates the system's insensitivity to sample axis rotation in the plane perpendicular to ranging of the laser light.
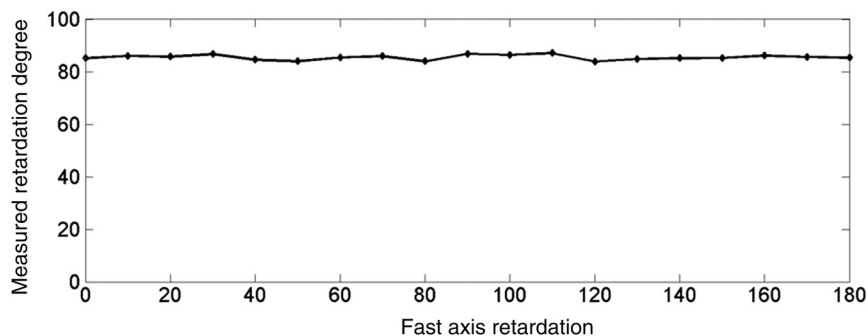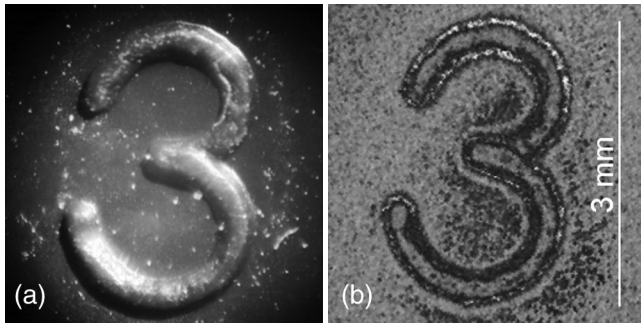

Fig. 2 Plot of measured retardance as a function of fast axis orientation.

Fig. 3 Co-registration image of engraved industrial plastic: (a) MMP and (b) PS-OCT.

The shared objective lens ensures that the PS-OCT and MMP systems are imaging the same region of interest. The co-registration of the systems was validated by constructing OCT *en face* images and comparing them to the MMP system. C-scans of $4 \times 4 \times 1.5$ mm ($256 \times 256 \times 520$ pixels) were generated by ImageJ (National Institutes of Health, Bethesda, Maryland) using a stack of B-scan OCT images collected at different lateral positions from the sample. *En face* images were then generated by extracting and summing signals within a constant depth (2 mm) of the three-dimensional data. Orientation of CCD camera for MMP and scanning voltage for PS-OCT is finely adjusted for the purpose of co-registration. Figure 3 shows the images from (a) PS-OCT and (b) MMP. In this example, the number 3 from a ruler was displayed at the same position in both images, demonstrating the spatially co-registration of two systems in a single platform. All images were smoothed with a 3×3 Gaussian filter.

2.2 *Biological Samples*

Heart leaflets were excised from baboon hearts donated from the Mannheimer Foundation which had previously euthanized the animals for reasons unrelated to our study. The hearts were stored in a $-80°$C freezer as tissue awaiting disposal before being acquired. Heart valve leaflets are highly birefringent due to their abundance of collagen fibrils. Changes in the concentration, or orientation of collagen fibrils within the leaflets, may cause alteration of the birefringence signature. Collagenase was selected in order to cause structural damage to the tissue. Chemical damage was induced by incubating a portion of the leaflet (2 mm $\times$ 2 mm $\times$ 0.5 mm) for 20 min in a solution of 0.14 g collagenase powder dissolved in 2.8 mL phosphate-buffered saline, 0.3 mL fetal bovine serum, and 0.3 mL antimicrobial solution at 37 °C. The experiment was used to demonstrate the sensitivity of PS-OCT-MMP to varying birefringence resulting from collagen contained in the leaflet. Birefringence maps were generated from the PS-OCT images, while Mueller matrix decomposition was performed on images taken by the MMP.

In a second set of experiments, freshly excised bovine tendons, obtained from the local abattoir, were extracted from the posterior side of the hind limbs. Tendon pieces were cut into strips measuring approximately 4 mm $\times$ 4 mm $\times$ 2 mm. Ultimately, change in the tendon structure was induced through thermal damage. A metal rod was heated at 260 °C and then put in contact with a tendon sample for a period of 2 s and for less than 0.5 s to achieve lower damage. The tendon samples were imaged to allow both the burned and the healthy sections to be visible simultaneously. Finally, tendon from the same animal was
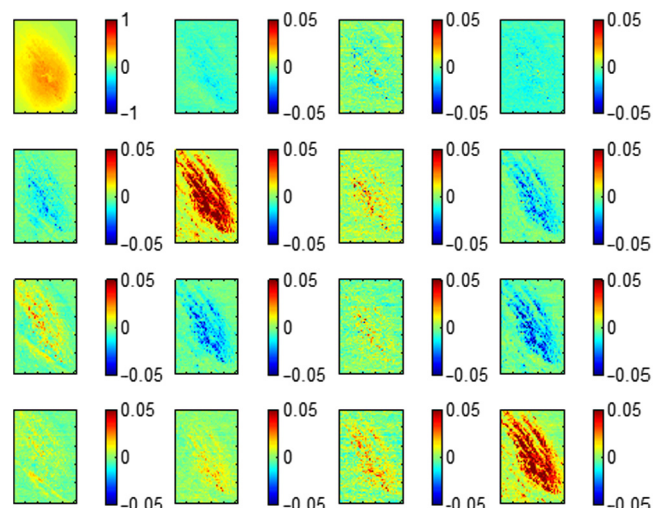
arranged on a rotational stage so that the axis of the sample could be rotated. Images were taken at -20 deg and $+60$ deg from the principal axis of our system, measured retardation was then compared within both systems.
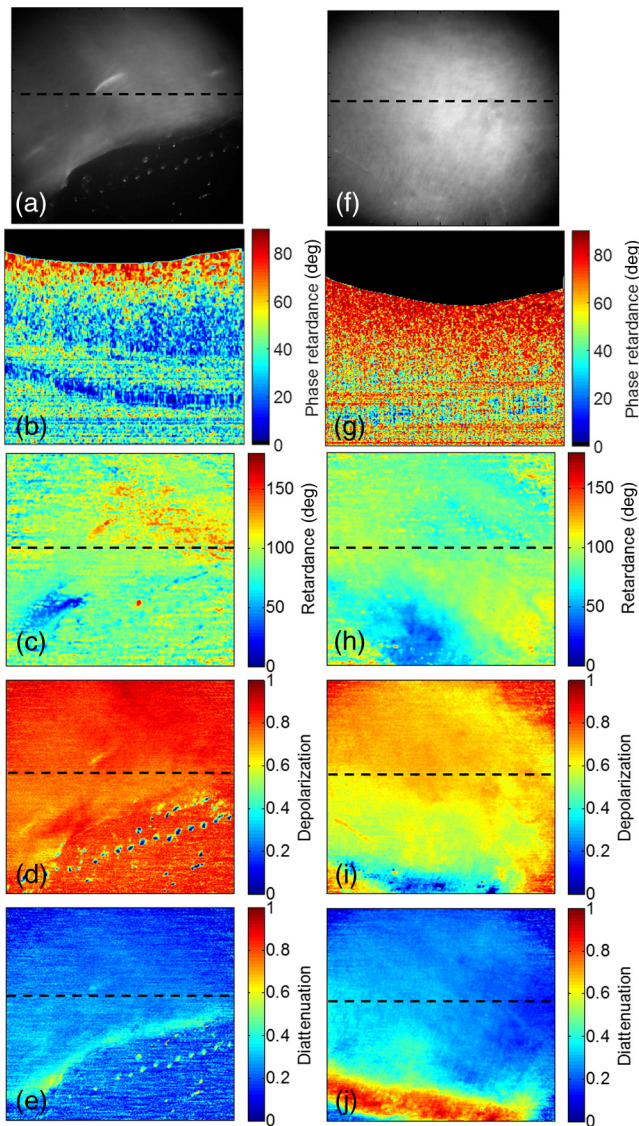
3 Results and Discussion

An example of a Mueller matrix image generated by our system is shown in Fig. 4 from imaging chicken tendon and shows similar patterns in Mueller matrix elements as presented by recent MMP of birefringent tissues. This can be seen as a symmetric pattern around the diagonal of the Mueller matrix with certain elements having reverse signs as discussed by He et al.[52] and Sun et al.[53]

3.1 *Heart Valve Leaflet*

Results of the Mueller matrix decomposition and PS-OCT imaging of heart valve leaflets are shown in Fig. 5. The black-dotted line indicates the location of the PS-OCT B-scans, and the dark spots oriented diagonally in Fig. 5(e) are water droplets located on the stage as seen in Fig. 5(a). Clear differences in the birefringence of the leaflet was observed between the fresh and collagenase deteriorated samples shown in Fig. 5. The depolarization values of the fresh leaflet are greater when compared with that of the deteriorated leaflet as shown on a scale of 0 to 1.0 in Figs. 5(d) and 5(i), 1.0 indicating a complete depolarization of the incident polarized light. The decrease in depolarization can be correlated with Figs. 5(b) and 5(g) which show PS-OCT B-scan images of the fresh leaflet and deteriorated leaflet, respectively. The PS-OCT image in Fig. 5(b) shows a half oscillation (i.e., the full oscillation is shown by a color change from red to blue and again to red), indicating a phase shift of ≈ 90 deg this is in contrast with Fig. 5(g) in the collagenase-treated sample, where the retardance is highly uniform throughout the deteriorated leaflet. This may be attributed to the loss of anisotropy and birefringence due to the randomization and destruction of collagen fibrils via collagenase activity. The destruction of the oscillatory pattern in phase retardance caused by loss of birefringence may explain the decrease in the depolarization effect of the tissue and can also be correlated with a loss of collagen content due to collagenase activity.[54–56] There is negligible difference between the Mueller matrix decomposed

Fig. 4 Mueller matrix of chicken tendon.

Fig. 6 Attenuation coefficient (solid), DOPU (dashed line), total depolarization (crossed line): (a) fresh leaflet and (b) damaged leaflet.

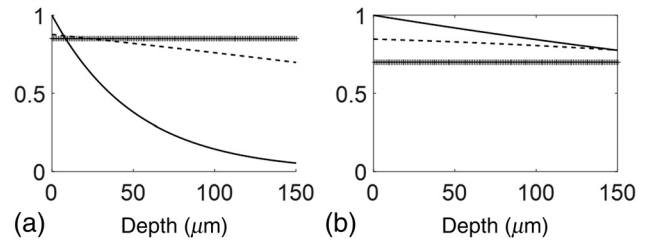

Fig. 5 Fresh leaflet: (a) CCD image, (b) PS-OCT B-scan phase retardance, (c) MM retardance, (d) depolarization, (e) diattenuation. Deteriorated leaflet: (f) CCD image, (g) PS-OCT B-scan, (h) MM retardance, (i) depolarization, and (j) diattenuation.

diattenuation between leaflet samples while in the retardance images some heterogeneous changes can be noticed particularly in the top portion of the figure. Calculation of the total depolarization obtained with MMP is finally related to the DOP uniformity (DOPU) introduced by Götzinger et al.[57] DOPU is expressed mathematically as resembling the expression for the DOP often used in optics.[1] Since PS-OCT is based on coherent light detection, the DOP is always equal to unity. The DOPU expression instead yields values $<= 1$, the main hypothesis being that by spatial averaging the local Stokes vectors of a sample concomitant speckles are also averaged.

$$DOPU = \sqrt{Q_{mean}^2 + U_{mean}^2 + V_{mean}^2}.$$

The calculation of the DOPU is achieved with a two-dimensional sliding average window in (x, z) directions. In our case, the window was 10 pixels × 10 pixels, similar to what was used by others.[58] The total depolarization of the treated and untreated

sample relates positively to the DOPU, as both metrics are higher in the untreated sample. While the total depolarization is cumulative the DOPU can be studied over depth as shown in Fig. 6. Similarly, we may calculate the attenuation coefficient for the samples. This is done utilizing the intensity image and then calculating the loss of intensity over depth, 50 pixels in the x directions were averaged to increase the SNR. The data were ultimately fit with an exponential function of the form $I \approx \sqrt{(e^{-2\mu_{tot}^L})}$ where μ_{tot} is the total attenuation coefficient and L is the depth of the sample, 2 is added to account for the round-trip travel.[59] In the figure, only the fitted data are shown (solid lines). In Fig. 6, we summarize the results of our quantitative analysis. Higher attenuation is expected to influence the total depolarization calculated through MMP. For the samples shown, the total attenuation coefficient was $\mu_{tot} = 9.6$ mm^{-1} for untreated leaflet and $\mu_{tot} = 0.6$ mm^{-1} for the treated leaflets. DOPU is lost at a higher rate in the untreated sample than the treated ones, indicating a higher depolarization ability of this sample, this is ultimately reflected in the Mueller matrix assessment of total depolarization [crosses in Figs. 6(a) and 5(d)] which is higher for untreated than treated samples.

3.2 Tendon

Fresh tendon is highly birefringent due to its collagen structure, its birefringence can be decreased through thermal damage. When the collagen in the tendon denatures due to heating, or other injuries, a decrease in birefringence can be observed. In PS-OCT of fresh tendon seen in Fig. 7(d), the banded structure, indicative of birefringence, is clearly visible to a depth of 750 μm and making full oscillations between 90 deg and 0 deg as polarized light travels deeper into the tissue. This is expected in tendon, which has high optical anisotropy. Figure 7(a) is a retardance image taken of fresh tendon by the MMP and shows some areas of greater retardance in an image with retardance mostly between 60 deg and 100 deg. Figure 7(b) is an *en face* image of the surface of the fresh tendon. The black-dotted line indicates the location of the PS-OCT B-scan in the MMP and OCT *en face* images. A strong and uniform pattern of phase retardance consistent with undamaged tendon can be seen around the burn site in Fig. 7(h). The image clearly shows a disappearance in the birefringence at the center of the burned zone. For comparison, Fig. 7(g) shows OCT image of the total backscattered intensity of the burned tendon. Less backscattered light from the burned area is observed. The colored bands changing around the burned area in Fig. 7(h) reveal important structural information not evident in the OCT B-scans of either tendon sample.

Figure 8 shows the tendon that was burned for 2 s while the superficially burned tendon is seen in Fig. 7. There is a clear difference between the samples. Seen in Fig. 8(a), the darkened
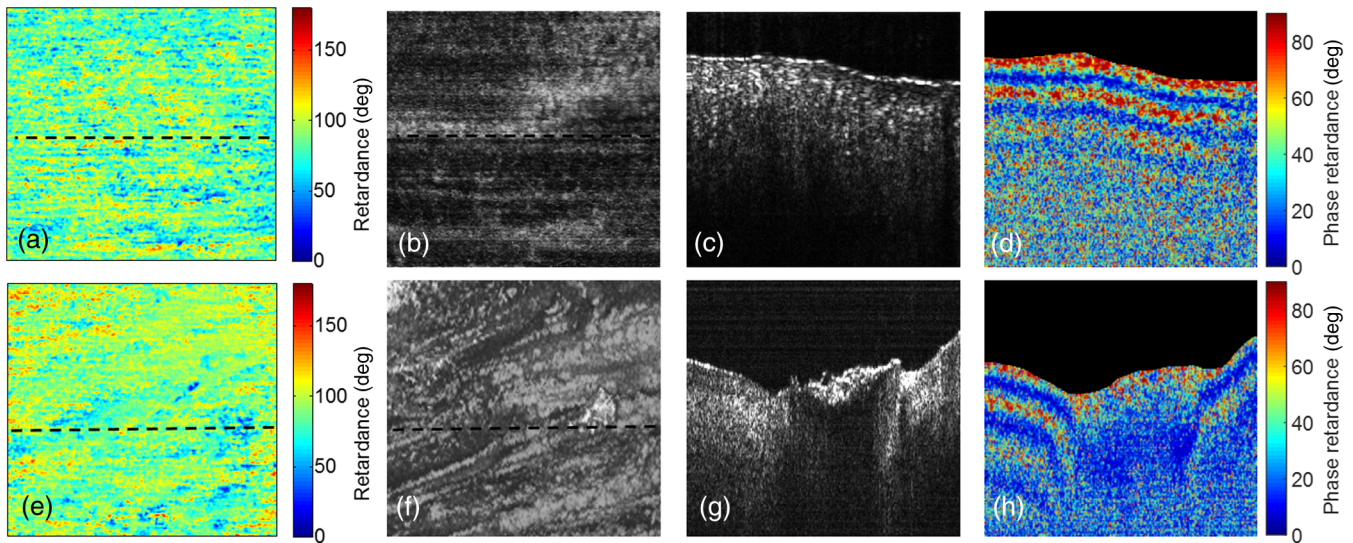
Fig. 7 Fresh bovine tendon: (a) MM retardance, (b) OCT *en face*, (c) OCT B-scan, and (d) PS-OCT B-scan. Superficially burned bovine tendon: (e) MM retardance, (f) OCT *en face*, (g) OCT B-scan, and (h) PS-OCT B-scan.

area at the center of the image and the area toward the bottom right of that section represent the locations where heat was applied. There is substantial increase in the diattenuation of the tendon in Fig. 8(b) where the darkened burn marks are present in the raw image. The actual burns themselves show a decrease in diattenuation compared to the rest of the image in focus and illuminated. Note that diattenuation relates to a material's favorable absorption of linearly polarized light in a specific orientation. The constriction of collagen fibers between the burns may factor in the area of heightened diattenuation. In the PS-OCT image of Fig. 8(e), a section of uniform phase retardance can be seen toward the right of the oscillating pattern typically exhibited by tendon. This section indicates the burned tissue similar to the burned tendon in Fig. 7. Figure 8(c) shows that there is a decrease in depolarization at the center of the burns.

Finally, Fig. 9 shows the results obtained with a chicken tendon sample oriented at two different orientations. The dotted line on the PS-OCT B-scans indicates where the data for the local phase retardation calculations were taken.

The chicken tendon showed in Fig. 9 reveals little change in the Mueller matrix decomposed retardance as the tendons orientation is changed beneath the sample objective shown in Figs. 9(a) and 9(c). This is also shown in the PS-OCT and corroborated in other work involving axis orientation and retardance.[60] The PS-OCT images of retardation show the typical oscillatory pattern, as the other bovine tendon samples. Local retardation was ultimately calculated with the algorithm by Jiao et al.[40] and proposed by others.[41] The results of the fit to the cumulative data are shown in Fig. 9. Using this approach, the sample is modeled as a stack of retarders within the imaging
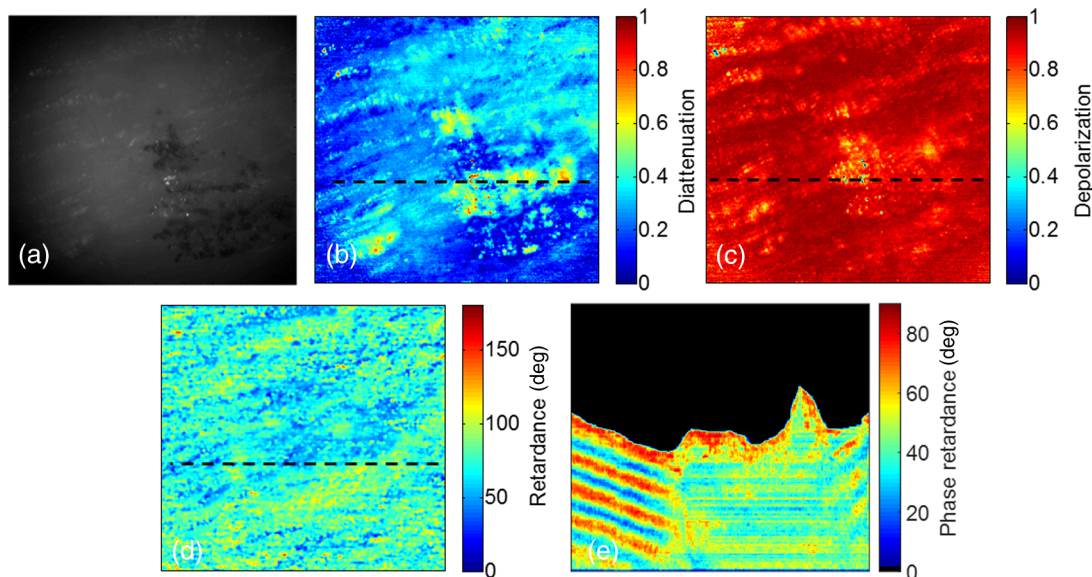
Fig. 8 Burned bovine tendon: (a) CCD image, (b) diattenuation, (c), depolarization, (d) MM retardance, and (e) PS-OCT B-scan.
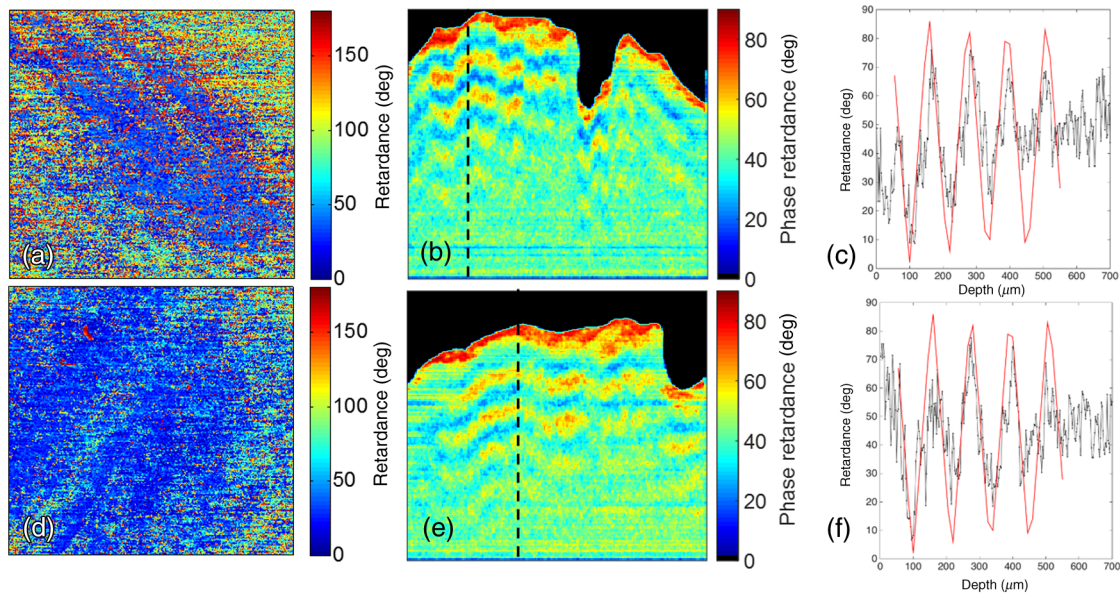
Fig. 9 (a) Chicken tendon MM retardance orientation 60 deg, (b) cumulative phase retardation, (c) local phase retardation data and model, (d) chicken tendon MM retardance orientation −20 deg, (e) cumulative phase retardation, and (f) local phase retardation data and model.

apparatus. The determination of the modeling retarder retardation and spacing is critical to this approach. In our calculation, the local retardation for the sample was calculated as 25 deg with each retarder being ∼30 μm in thickness. In comparison, the cumulative retardation obtained with the Mueller matrix is in the range of 25 deg to 35 deg. Further work remains to be done to truly understand how the two measurements relate to each other.

4 Conclusion

We have introduced a combined PS-OCT-MMP and illustrated how this multimodal imaging technique can provide structural information about tissues using heart valve leaflets and tendon. Damage of leaflet structure with collagenase was identified by decomposing the depolarization parameter of the Mueller matrix, showing the tissue had less of a randomizing (lower attenuation coefficient) effect on polarized light backscattered from the leaflet. Several authors are using the DOPU for automatic segmentation of the retinal pigmented epithelium[57,58] and other depolarizing structures. This seems counterintuitive, as the Jones calculus does not account for depolarization yet these authors consider the random polarization state of the resulting speckle as causing the DOP to be lower than 1. With our approach, the true depolarizing property of a sample calculated through the decomposition of the Mueller matrix was related to the PS-OCT DOP. Not only the DOP and DOPU were consistent for the samples under study but also their behavior seems to relate to the attenuation coefficient and the scattering property of the material that can be extrapolated through PS-OCT. We acknowledge the fact that on layered structures such as the retina the localization of the depolarization is not feasible without a robust inverse model, nevertheless this is a first attempt at relating the DOPU and DOP directly.

Areas of thermal damage to tendon were also observed by decomposing the diattenuation and depolarization components of the Mueller matrix in the deeper burned sample. Changes in the normal retardance pattern of tendon were identified where large changes in depolarization and diattenuation were seen in the more severely burned tendon. It was expected that significant damage to birefringent tissue would change its effect on polarized light as normal structure and scattering profile is lost. This experiment shows how PS-OCT could be used to corroborate Mueller matrix results as they could show changes in material properties at different depth that are not visible through wide-field imaging. Finally, the last example in Fig. 8 shows another potential application of this approach. Both MMP (in back reflectance) and PS-OCT can provide measurement of cumulative retardation of a sample and birefringence. In PS-OCT, models have been proposed to convert the cumulative retardation into local retardation[39] yet true quantification of this parameter seems elusive. The combined approach could be utilized to refine models of local retardation, particularly as many models rely on the measurement of the surface retardation as a starting point for the model.[41] Naturally, this would require a clear understanding of the Mueller matrix sampling depth, as well as uniform and well-calibrated samples ultimately combined with computational approach. In conclusion, we believe this combined approach is a starting point in obtaining more quantifiable PS-OCT measurement at the same time we believe PS-OCT could be used in this combined system to better understand Mueller matrix decomposition results. Further work is needed to achieve both goals.

References

1. N. Ghosh and I. A. Vitkin, "Tissue polarimetry: concepts, challenges, applications, and outlook," *J. Biomed. Opt.* **16**, 110801 (2011).

2. S. L. Jacques, J. C. Ramella-Roman, and K. Lee, "Imaging skin pathology with polarized light," *J. Biomed. Opt.* **7**, 329–340 (2002).
3. S. G. Demos and R. R. Alfano, "Optical polarization imaging," *Appl. Opt.* **36**, 150–155 (1997).
4. S. G. Demos et al., "Polarization filter for biomedical tissue optical imaging," *Photochem. Photobiol.* **66**, 821–825 (1997).
5. S. P. Morgan and I. M. Stockford, "Surface-reflection elimination in polarization imaging of superficial tissue," *Opt. Lett.* **28**, 114–116 (2003).
6. M. F. Wood, X. Guo, and I. A. Vitkin, "Polarized light propagation in multiply scattering media exhibiting both linear birefringence and optical activity: Monte Carlo model and experimental methodology," *J. Biomed. Opt.* **12**, 014029 (2007).
7. S. Demos, H. Radousky, and R. Alfano, "Deep subsurface imaging in tissues using spectral and polarization filtering," *Opt. Express* **7**, 23–28 (2000).
8. B. Kunnen et al., "Application of circularly polarized light for non-invasive diagnosis of cancerous tissues and turbid tissue-like scattering media," *J. Biophotonics* **8**, 317–323 (2015).
9. T. Yun et al., "Monte Carlo simulation of polarized photon scattering in anisotropic media," *Opt. Express* **17**, 16590–16602 (2009).
10. J. Ramella-Roman, S. Prahl, and S. Jacques, "Three Monte Carlo programs of polarized light transport into scattering media: part I," *Opt. Express* **13**, 4420–4438 (2005).
11. K. M. Myers et al., "The mechanical role of the cervix in pregnancy," *J. Biomech.* **48**, 1511–1523 (2015).
12. H. C. Wells et al., "Collagen fibril structure and strength in acellular dermal matrix materials of bovine, porcine, and human origin," *ACS Biomater. Sci. Eng.* **1**, 1026–1038 (2015).
13. J. C. Ramella-Roman et al., "Preferential alignment of birefringent tissue measured with polarization sensitive techniques," *Proc. SPIE* **9303**, 93030I (2015).
14. S. Sugita and T. Matsumoto, "Quantitative measurement of the distribution and alignment of collagen fibers in unfixed aortic tissues," *J. Biomech.* **46**, 1403–1407 (2013).
15. W. F. Cheong, S. A. Prahl, and A. J. Welch, "A review of the optical properties of biological tissues," *IEEE J. Quantum Electron.* **26**, 2166–2185 (1990).
16. A. Pierangelo et al., "Ex vivo photometric and polarimetric multilayer characterization of human healthy colon by multispectral Mueller imaging," *J. Biomed. Opt.* **17**, 066009 (2012).
17. A. Pierangelo et al., "Multispectral Mueller polarimetric imaging detecting residual cancer and cancer regression after neoadjuvant treatment for colorectal carcinomas," *J. Biomed. Opt.* **18**, 046014 (2013).
18. P. J. Wu and J. T. Walsh, "Stokes polarimetry imaging of rat-tail tissue in a turbid medium using incident circularly polarized light," *Lasers Surg. Med.* **37**, 396–406 (2005).
19. N. Ghosh, M. F. Wood, and I. A. Vitkin, "Mueller matrix decomposition for extraction of individual polarization parameters from complex turbid media exhibiting multiple scattering, optical activity, and linear birefringence," *J. Biomed. Opt.* **13**, 044036 (2008).
20. J. Dillet et al., "Size determination by use of two-dimensional Mueller matrices backscattered by optically thick random media," *Appl. Opt.* **45**, 4669–4678 (2006).
21. S. Y. Lu and R. A. Chipman, "Interpretation of Mueller matrices based on polar decomposition," *J. Opt. Soc. Am. A* **13**, 1106–1113 (1996).
22. M. R. Antonelli et al., "Mueller matrix imaging of human colon tissue for cancer diagnostics: how Monte Carlo modeling can help in the interpretation of experimental data," *Opt. Express* **18**, 10200–10208 (2010).
23. A. Pierangelo et al., "Ex-vivo characterization of human colon cancer by Mueller polarimetric imaging," *Opt. Express* **19**, 1582–1593 (2011).
24. P. Shukla and A. Pradhan, "Mueller decomposition images for cervical tissue: Potential for discriminating normal and dysplastic states," *Opt. Express* **17**, 1600–1609 (2009).
25. K. H. Kim et al., "In vivo imaging of human burn injuries with polarization-sensitive optical coherence tomography," *J. Biomed. Opt.* **17**, 066012 (2012).
26. J. C. Ramella-Roman, S. A. Prahl, and S. L. Jacques, "Three Monte Carlo programs of polarized light transport into scattering media: part II," *Opt. Express* **13**, 10392–10405 (2005).
27. I. Meglinski et al., "Simulation of polarization-sensitive optical coherence tomography images by a Monte Carlo method," *Opt. Lett.* **33**, 1581–1583 (2008).
28. J. A. Izatt et al., "Optical coherence tomography and microscopy in gastrointestinal tissues," *IEEE J. Sel. Top. Quantum Electron.* **2**, 1017–1028 (1996).
29. M. Wojtkowski et al., "Ultrahigh-resolution, high-speed, Fourier domain optical coherence tomography and methods for dispersion compensation," *Opt. Express* **12**, 2404–2422 (2004).
30. A. M. Zysk et al., "Optical coherence tomography: a review of clinical development from bench to bedside," *J. Biomed. Opt.* **12**, 051403 (2007).
31. B. J. Vakoc et al., "Cancer imaging by optical coherence tomography: preclinical progress and clinical potential," *Nat. Rev. Cancer* **12**, 363–368 (2012).
32. P. F. Lee et al., "Angiogenic responses are enhanced in mechanically and microscopically characterized, microbial transglutaminase crosslinked collagen matrices with increased stiffness," *Acta Biomater.* **9**, 7178–7190 (2013).
33. H. C. Gibbs et al., "Imaging embryonic development with ultrashort pulse microscopy," *Opt. Eng.* **53**, 051506 (2013).
34. H. C. Gibbs et al., "Combined lineage mapping and gene expression profiling of embryonic brain patterning using ultrashort pulse microscopy and image registration," *J. Biomed. Opt.* **19**, 126016 (2014).
35. Y. Q. Bai et al., "Dynamic multicomponent engineered tissue reorganization and matrix deposition measured with an integrated nonlinear optical microscopy-optical coherence microscopy system," *J. Biomed. Opt.* **19**, 036014 (2014).
36. Y. Q. Bai et al., "Sequential multimodal microscopic imaging and biaxial mechanical testing of living multicomponent tissue constructs," *Ann. Biomed. Eng.* **42**, 1791–1805 (2014).
37. J. A. Burns et al., "Polarization-sensitive optical coherence tomography imaging of benign and malignant laryngeal lesions: an in vivo study," *Otolaryngol. Head Neck Surg.* **145**, 91–99 (2011).
38. S. Jiao et al., "Fiber-based polarization-sensitive Mueller matrix optical coherence tomography with continuous source polarization modulation," *Appl. Opt.* **44**, 5463–5467 (2005).
39. S. Jiao and L. V. Wang, "Two-dimensional depth-resolved Mueller matrix of biological tissue measured with double-beam polarization-sensitive optical coherence tomography," *Opt. Lett.* **27**, 101–103 (2002).
40. S. Jiao et al., "Contrast mechanisms in polarization-sensitive Mueller-matrix optical coherence tomography and application in burn imaging," *Appl. Opt.* **42**, 5191–5197 (2003).
41. C. Fan and G. Yao, "Mapping local optical axis in birefringent samples using polarization-sensitive optical coherence tomography," *J. Biomed. Opt.* **17**, 110501 (2012).
42. C. Fan and G. Yao, "Imaging myocardial fiber orientation using polarization sensitive optical coherence tomography," *Biomed. Opt. Express* **4**, 460–465 (2013).
43. Y. Fukuma et al., "Retinal nerve fiber layer retardation measurements using a polarization-sensitive fundus camera," *J. Biomed. Opt.* **16**, 076017 (2011).
44. S. Makita et al., "Degree of polarization uniformity with high noise immunity using polarization-sensitive optical coherence tomography," *Opt. Lett.* **39**, 6783–6786 (2014).
45. S. W. Lee et al., "Quantification of scattering changes using polarization-sensitive optical coherence tomography," *J. Biomed. Opt.* **13**, 054032 (2008).
46. K. L. Lurie, T. J. Moritz, and A. K. Ellerbee, "Design considerations for polarization-sensitive optical coherence tomography with a single input polarization state," *Biomed. Opt. Express* **3**, 2273–2287 (2012).
47. L. X. Chin et al., "En face parametric imaging of tissue birefringence using polarization-sensitive optical coherence tomography," *J. Biomed. Opt.* **18**, 066005 (2013).
48. M. Yamanari, S. Makita, and Y. Yasuno, "Polarization-sensitive swept-source optical coherence tomography with continuous source polarization modulation," *Opt. Express* **16**, 5892–5906 (2008).
49. B. Boulbry, J. C. Ramella-Roman, and T. A. Germer, "Improved method for calibrating a Stokes polarimeter," *Appl. Opt.* **46**, 8533–8541 (2007).
50. P. Ghassemi et al., "A new approach for optical assessment of directional anisotropy in turbid media," *J. Biophotonics* **9**, 100–108 (2016).
51. B. Boulbry, J. C. Ramella-Roman, and T. A. Germer, "Improved method for calibrating a Stokes polarimeter," *Appl. Opt.* **46**, 8533–8541 (2007).
52. C. He et al., "Quantitatively differentiating microstructures of tissues by frequency distributions of Mueller matrix images," *J. Biomed. Opt.* **20**, 105009 (2015).

53. M. Sun et al., "Characterizing the microstructures of biological tissues using Mueller matrix and transformed polarization parameters," *Biomed. Opt. Express* **5**, 4223–4234 (2014).

54. M. F. G. Wood et al., "Proof-of-principle demonstration of a Mueller matrix decomposition method for polarized light tissue characterization in vivo," *J. Biomed. Opt.* **14**, 014029 (2009).

55. S. K. Nadkarni et al., "Measurement of collagen and smooth muscle cell content in atherosclerotic plaques using polarization-sensitive optical coherence tomography," *J. Am. Coll. Cardiol.* **49**, 1474–1481 (2007).

56. M. E. Brezinski, *Optical Coherence Tomography: Principles and Applications*, Chapter 16.1, pp. 462–472, Academic Press, Burlington, MA (2006).

57. E. Gotzinger et al., "Retinal pigment epithelium segmentation by polarization sensitive optical coherence tomography," *Opt. Express* **16**, 16410–16422 (2008).

58. M. Sugita et al., "Analysis of optimum conditions of depolarization imaging by polarization-sensitive optical coherence tomography in the human retina," *J. Biomed. Opt.* **20**, 016011 (2015).

59. E. C. C. Cauberg et al., "Quantitative measurement of attenuation coefficients of bladder biopsies using optical coherence tomography for grading urothelial carcinoma of the bladder," *J. Biomed. Opt.* **15**, 066013 (2010).

60. Z. Lu, D. Kasaragod, and S. J. Matcher, "Conical scan polarization-sensitive optical coherence tomography," *Biomed. Opt. Express* **5**, 752–762 (2014).

Joseph Chue-Sang received his BS degree in biomedical engineering from Florida International University in 2013. He is a PhD student in biomedical engineering at Florida International University under Dr. Jessica C. Ramella-Roman. He is interested in imaging of birefringent tissues using modalities such as Mueller matrix polarimetry and polarization sensitive optical coherence tomography.

Yuqiang Bai received his BS in physics from Shanxi University in 1999 and his MS in optics from Shanghai Jiao Tong University in 2002. He completed his PhD in biomedical engineering from Texas A&M University at College Station in 2014. Currently, he is a visiting postdoc associate in the Department of Biomedical Engineering at Florida International University, where he developed polarization sensitive optical coherence tomography and two photon fluorescence microscopy systems to study anisotropic biological tissue.

Jessica C. Ramella-Roman received an electrical engineering degree from the University of Pavia, Italy, and a MS and PhD degree also in electrical engineering from Oregon Health Science University in Portland, Oregon. She was a postdoctoral fellow at Johns Hopkins University and then an assistant professor and associate professor at Catholic University in Washington, DC, from 2005 to 2013. Since 2013, she has been an associate professor at Florida International University in Miami, Florida.

Biographies for the other authors are not available.